A simplified coronary model for diagnosis of ischemia-causing coronary stenosis

Yili Feng[a], Bao Li[a], Ruisen Fu[a], Yaodong Hao[a], Tongna Wang[a], Huanmei Guo[a], Junling Ma[a], Gerold Baier[b], Haisheng Yang[a], Quansheng Feng[c], Liyuan Zhang[a],*, Youjun Liu[a],*

[a] Department of Biomedical Engineering, Faculty of Environment and Life, Beijing University of Technology, No. 100 Pingleyuan, Chaoyang District, Beijing 100124, China.
[b] Cell and Developmental Biology, University College London, London, WC1E 6BT, UK
[c] Department of Cardiology, the First People's Hospital of Guangshui, Guangshui Hubei 432700, China.

*** Corresponding Author:**
Youjun Liu, Email: lyjlma@bjut.edu.cn.
Liyuan Zhang, Email: LiyuanZhang@bjut.edu.cn.

Category of the Manuscript: Original Article

Abstract

Background and Objective: The functional assessment of the severity of coronary stenosis from coronary computed tomography angiography (CCTA)-derived fractional flow reserve (FFR) has recently attracted interest. However, existing algorithms run at high computational cost. Therefore, this study proposes a fast calculation method of FFR for the diagnosis of ischemia-causing coronary stenosis.

Methods: We combined CCTA and machine learning to develop a simplified single-vessel coronary model for rapid calculation of FFR. First, a zero-dimensional model of single-vessel coronary was established based on CCTA, and microcirculation resistance was determined through the relationship between coronary pressure and flow. In addition, a coronary stenosis model based on machine learning was introduced to determine stenosis resistance. Computational FFR (cFFR) was then obtained by combining the zero-dimensional model and the stenosis model with inlet boundary conditions for resting ($cFFR_r$) and hyperemic ($cFFR_h$) aortic pressure, respectively. We retrospectively analyzed 75 patients who underwent clinically invasive FFR (iFFR), and verified the model accuracy by comparison of cFFR with iFFR.

Results: The average computing time of cFFR was less than 2 seconds. The correlations between $cFFR_r$ and $cFFR_h$ with iFFR were $r = 0.89$ ($p < 0.001$) and $r = 0.90$ ($p < 0.001$), respectively. Diagnostic accuracy, sensitivity, specificity, positive predictive value, negative predictive value, positive likelihood ratio, negative likelihood ratio for $cFFR_r$ and $cFFR_h$ were 90.7%, 95.0%, 89.1%, 76.0%, 98.0%, 8.7, 0.1 and 92.0%, 95.0%, 90.9%, 79.2%, 98.0%, 10.5, 0.1, respectively.

Conclusions: The proposed model enables rapid prediction of cFFR and exhibits high diagnostic performance in selected patient cohorts. The model thus provides an accurate and time-efficient computational tool to detect ischemia-causing stenosis and assist with clinical decision-making.

Keywords: fractional flow reserve, coronary computed tomography angiography, coronary zero-dimensional model, machine learning, coronary stenosis model

Abbreviations

CCTA: coronary computed tomography angiography; FFR: fractional flow reserve; CFD: computational fluid dynamics; CT-FFR: fractional flow reserve derived from coronary computed tomography angiography; TAG: transluminal attenuation gradient; iFFR: invasive fractional flow reserve; ML: machine learning; $P_{a\text{-}res}$: resting aortic pressure; $P_{a\text{-}hyp}$: hyperemic aortic pressure; cFFR: computational fractional flow reserve; ICA: invasive coronary angiography; $R_{m\text{-}res}$: resting microcirculation resistance; MAP: mean arterial pressure; SBP: systolic blood pressure; DBP: diastolic blood pressure; $R_{m\text{-}hyp}$: hyperemic microcirculation resistance; MAP_{res}: resting mean arterial pressure; MAP_{hyp}: hyperemic mean arterial pressure; P_a: aortic pressure; BPNN: back-propagation neural network; P_d: distal coronary pressure; $cFFR_r$: cFFR with resting aortic pressure as inlet boundary conditions; $cFFR_h$, cFFR with hyperemic aortic pressure as inlet boundary conditions; SD: standard deviation; ROC: receiver operating characteristic; AUC: area under the receiver operating characteristic curve; PPV:

positive predictive value; NPV: negative predictive value; LR+: positive likelihood ratio; LR−: negative likelihood ratio; CI: confidence interval.

1. Introduction

It was found that the relationship between coronary stenosis and myocardial ischemia is complex [1]. The results showed that 35% of patients with a stenosis of 50-70% are ischemic; while 20% of patients with a stenosis of 71-90% are not ischemic [2]. Thus, it is particularly important to quantify the relationship between coronary stenosis and myocardial ischemia. Coronary computed tomography angiography (CCTA) can identify the anatomical severity of stenosis, but cannot evaluate the functional significance of stenosis, that is, whether the stenosis is causing ischemia [1]. Currently, the gold standard for functional assessment of myocardial ischemia is fractional flow reserve (FFR) [3], which is defined as the ratio of the maximum hyperemic flow through a stenotic artery to the maximum hyperemic flow under the assumption that the artery is normal [4]. Studies have manifested that FFR is of great significance in the diagnosis and treatment of functional stenosis, improving outcomes and reducing major adverse cardiac events [5–7]. Nevertheless, the measurement of FFR requires pressure wire and intravenous adenosine, prolonging the operation time and increasing the short-term cost, which limits its widespread clinical utility [8].

In recent years, the application of computational fluid dynamics (CFD) has made the noninvasive computation of FFR derived from CCTA (CT-FFR) possible [4,9,10]. The recognized CT-FFR (Heartflow) adopted a mathematical model, which combines a coronary anatomical model with a coronary physiological model, and uses CFD to solve the governing equation (a three-dimensional Navier-Stokes equation) for coronary pressure and flow during hyperemia [9,11]. The diagnostic performance of CT-FFR has been verified in three prospective multicenter controlled trials [12–14]. Studies have suggested that CT-FFR has good diagnostic accuracy (73%-87.4%) with invasive FFR as the reference standard [12–14]. Compared with CCTA alone, CT-FFR exhibits higher diagnostic accuracy in distinguishing ischemic and non-ischemic stenosis (84.3% vs 58.5%) [12]. Yet, the Navier-Stokes equation describing the blood flow in CT-FFR computation is a system of nonlinear partial differential equations, which is very time-consuming to solve. It usually takes several hours (1-6 h) to analyze CT-FFR on a parallel supercomputer [12–14]. Therefore, alternative CT-FFR techniques that allow rapid execution are needed.

Many studies have been carried out on the fast computing of CT-FFR, mainly including Siemens [15,16], Toshiba [17], United-Imaging [18] and so on. Siemens Healthcare used a hybrid approach to model blood flow, and enabled fast computation of CT-FFR by coupling reduced-order and full-order models [19]. This simplified calculation method has a good diagnostic accuracy [15]. In addition, Toshiba Medical developed a method using 4D-CT image tracking and structural and fluid analysis to quickly estimate CT-FFR [20,21]. The results demonstrated that the proposed 4D-CT-FFR analysis approach has the potential to evaluate the effect of coronary stenosis on blood flow [17]. Furthermore, Siemens Healthcare presented a machine-learning-based model for predicting CT-FFR as an alternative to physics-based approaches [22]. There was an excellent correlation between the machine-learning and the physics-based predictions [16]. Recently, United-Imaging Healthcare proposed a CT-FFR approach using the transluminal attenuation gradient (TAG) of each coronary to obtain the outlet boundary conditions, which also manifested good diagnostic performance in detecting ischemia-causing stenosis [18]. Although compared with Heartflow CT-FFR, these fast calculation methods have greatly reduced the computational cost. Nevertheless, apart from the time spent on coronary segmentation, the computing time of FFR still requires 5-15 min [15–18], which may still not meet the clinical timeliness requirements.

On the premise of ensuring the relative accuracy of the three-dimensional reconstruction, this study proposed a fast CT-FFR calculation method with a single-vessel coronary as the region of interest, which has high accuracy compared with clinically measured invasive FFR (iFFR). We simplified the coronary three-dimensional model derived from CCTA to a single-vessel coronary zero-dimensional model (circuit model), and took the stenotic single-vessel coronary artery as the region of interest to reduce the computational cost. The zero-dimensional model has been widely used in the modeling of cardiovascular mechanics [23–28]. However, the simplified zero-dimensional model will lose the local geometric features of the three-dimensional model. Machine learning (ML) algorithms allow a wealth of information to be extracted from data that can be transformed into knowledge about the underlying fluid mechanics [29,30]. Hence, we trained and learned the geometric features of a large number of three-dimensional models through ML, and established a coronary stenosis model that can represent the geometric characteristics of blood vessels. Finally, the stenosis model was embedded into the simplified zero-dimensional model to ensure the accuracy of the model. In addition, we considered and compared the effects of resting aortic pressure ($P_{a\text{-}res}$) and hyperemic aortic pressure ($P_{a\text{-}hyp}$) as inlet boundary conditions on the accuracy of the model. The accuracy of the simplified model was validated by comparison the computational FFR (cFFR) simulated in this study with the iFFR. This simplified model presented for rapid prediction of FFR may be suitable for clinical timeliness requirements, which has potential application value for the diagnosis of ischemia-causing coronary stenosis.

2. Methods

2.1 Study Population

This was a single-center, retrospective study conducted at the Peking University People's Hospital. A total of 75 stable patients with suspected or known coronary artery disease who had undergone CCTA, invasive coronary angiography (ICA) and iFFR measurements between March 2019 and May 2021 were enrolled. All patients were low to intermediate risk patients with visual stenosis ranging from 30% to 90%, and the diameter of vessels was ≥ 2 mm. Patients were excluded if they had a history of contraindication to adenosine, prior percutaneous coronary intervention, coronary artery bypass grafting surgery, or inability to adhere to study procedures. This study was in line with the principles of the Declaration of Helsinki and approved by the Medical Ethics Committee of Peking University People's Hospital. Informed written consent was received from all patients participating in this study.

2.2 Clinical Experiments

CCTA was performed using a 256-row detector CT system. The scan parameters were: collimation 256 × 0.625 mm, gantry rotation time 280 ms, tube voltage 100 or 120 kV, and tube current 300 to 500 mA. The matrix size was 512 × 512 pixels and the pixel size within each slice was 0.5 mm × 0.5 mm. Images were reconstructed with a slice thickness of 0.625 mm under the guidance of clinical cardiologists. ICA and iFFR measurements were carried out in accordance with standard practice. The pressure wire was positioned a minimum of 20 mm distal to the stenosis [18]. Maximal hyperemia was induced by intravenous administration of adenosine (140 μg/kg/min) [4]. FFR was calculated by dividing the mean distal coronary pressure by the mean aortic pressure during maximal hyperemia [31,32], and an FFR of < 0.80 was considered hemodynamically significant.

2.3 cFFR Computation

Computation of cFFR requires reconstruction of a coronary anatomical model to extract geometric information; establishment of a coronary physiological model to derive boundary conditions representing cardiac output, aortic pressure, and microcirculation resistance; and application of CFD to solve the governing equations. This combination of anatomy, physiology, and CFD makes it possible to compute coronary pressure and flow.

In the current study, we adopted a coronary zero-dimensional model to simulate normal, healthy coronary arteries. In addition, the coronary stenosis model based on ML we developed previously was introduced to simulate the stenosis resistance produced by the stenotic segment. Such a simplified approach enables rapid and accurate prediction of pressure and flow in patient-specific coronary models.

2.3.1 Model Preprocessing

2.3.1.1 Coronary Anatomy Model

The reconstruction and segmentation of coronary anatomical model (including the measurement of geometric parameters) was carried out using Mimics Research version 20.0 under the guidance of clinical cardiologists, which ensures the accuracy of the three-dimensional model. First, the patient-specific coronary anatomical model (**Fig. 1A**) was reconstructed from CCTA images. The topology of the coronary tree was then extracted from the anatomical model, and the geometric parameters of the coronary artery were manually measured, including vessel length, vessel diameter and vessel cross-sectional area. Moreover, the coronary artery in which the stenosis was located was identified and segmented, and the geometric parameters related to the stenotic coronary artery were measured, including stenosis entrance length, stenosis exit length, stenosis minimum length, stenosis entrance area and stenosis minimum area (**Fig. 1B**). In the current study, geometric parameters such as the length, diameter, and cross-sectional area of normal and healthy coronary arteries were used to establish a personalized coronary zero-dimensional model, while the geometric parameters related to stenotic coronary arteries were used to establish a personalized coronary stenosis model.

2.3.1.2 Coronary Physiological Model

The coronary physiological model (**Fig. 2**) was derived from patient-specific data with 3 main principles: 1) resting coronary flow is proportional to cardiac output; 2) microcirculation resistance is inversely proportional to vessel diameter; and 3) microcirculation resistance is reduced to simulate maximal hyperemia [4].

Principle 1: Resting coronary flow is proportional to cardiac output.

Total coronary flow was estimated from clinically measured cardiac output [23]:

$$Q_{cor}=CO\cdot 4\% \tag{1}$$

where Q_{cor} represents total coronary flow and CO represents cardiac output. At rest, the flow rate of left and right coronary artery accounted for 60% and 40% of total coronary flow, respectively [4]. According to the allometric scaling law we took $Q \propto d^3$ [9] to determine the flow rate of each coronary artery, where Q represents coronary flow and d represents vessel diameter.

Principle 2: Microcirculation resistance is inversely proportional to vessel diameter.

The quantification of resting microcirculation resistance ($R_{m\text{-}res}$) mainly includes the following 5 steps.

1) Resistance, current and voltage simulate flow resistance, flow rate and blood pressure, respectively. Assuming that the coronary artery was healthy and normal, the coronary resistance was computed according to the measured geometric parameters:

$$R=\frac{8\pi\mu L}{A^2} \tag{2}$$

where R is the coronary resistance, μ is the dynamic viscosity with a value of 0.0035 (Pa s), L is the vessel length, and A is the vessel cross-sectional area.

2) Aortic pressure was estimated by mean arterial pressure (MAP), which was obtained from clinically measured resting systolic blood pressure (SBP) and diastolic blood pressure (DBP) [33]:

$$MAP=\frac{SBP+2\cdot DBP}{3} \tag{3}$$

3) The coronary nodal pressure was calculated by coronary resistance and coronary flow:

$$P_{down}=P_{up}-R\cdot Q \tag{4}$$

where P_{down} is the next node pressure of the coronary artery, and P_{up} is the previous node pressure of the coronary artery. For example, for the coronary artery between Node 1 and Node

2 (**Fig. 3**), P_{down} represents the pressure at Node 2 (P_2), and P_{up} represents the pressure at Node 1 (P_1).

4) The coronary outlet pressure was determined from coronary nodal pressure, coronary resistance and coronary flow:

$$P_{out}=P_{up}-R\cdot Q \tag{5}$$

where P_{out} is the coronary outlet pressure. For example, for the coronary artery between Node 1 and Outlet 1a (**Fig. 3**), P_{out} is the pressure at Outlet 1a (P_{1a}), and P_{up} is the pressure at Node 1 (P_1).

5) The resting microcirculation resistance was estimated according to the coronary outlet pressure and coronary flow [34].

$$R_{m\text{-}res}=\frac{P_{out}}{Q} \tag{6}$$

Therefore, $Q \propto d^3$ implies that $R_{m\text{-}res} \propto d^{-3}$, or that the microcirculation resistance is inversely proportional to the vessel diameter [9].

Principle 3: Microcirculation resistance is reduced to simulate maximal hyperemia.

The resting microcirculation resistance was reduced by 0.24 times to simulate the hyperemic microcirculation resistance ($R_{m\text{-}hyp}$) [4].

$$R_{m\text{-}hyp}=R_{m\text{-}res}\cdot 0.24 \tag{7}$$

2.3.1.3 Boundary Condition

Previous studies used aortic pressure estimated by MAP as the inlet boundary condition [9,35]. Since the result obtained by formula (3) is the resting MAP (MAP_{res}), the estimated aortic pressure here is $P_{a\text{-}res}$. Nevertheless, the measurement of FFR was carried out in the hyperemic state, so two inlet boundary conditions, $P_{a\text{-res}}$ and $P_{a\text{-hyp}}$, were considered in this study. Considering that the $P_{a\text{-hyp}}$ was unable to be obtained directly, we counted the MAP_{res} and hyperemic MAP (MAP_{hyp}) obtained by invasive measurement in 89 patients. It was found that MAP_{hyp} (82.19 ± 11.80 mmHg) was approximately 0.81 times of the MAP_{res} (100.98 ± 13.50 mmHg). This was consistent with the estimate of $P_{a\text{-hyp}}$ by 0.8 times of $P_{a\text{-res}}$ described in the literature [18]. Accordingly, we simulated $P_{a\text{-hyp}}$ by 0.81 times of MAP_{res}.

2.3.2 Coronary Zero-Dimensional Model

The model parameters obtained in *Section 2.3.1* were used to establish the personalized coronary zero-dimensional model. The stenotic single-vessel coronary artery was taken as the region of interest (**Fig. 4A**). $P_{a\text{-res}}$ and $P_{a\text{-hyp}}$ were respectively set as the inlet boundary conditions, and the $R_{m\text{-hyp}}$ was set as the outlet boundary condition. Thus, the personalized coronary zero-dimensional model for simulating hyperemia is (**Fig. 4B**):

$$Q_s = \frac{P_a}{R_{m\text{-hyp}} + R_s} \tag{8}$$

where Q_s is hyperemic coronary flow, P_a is aortic pressure, and R_s is stenosis resistance. For the personalized coronary zero-dimensional model, P_a and $R_{m\text{-hyp}}$ are constant, while hyperemic coronary flow changes with the change of stenosis resistance. Hence, the coronary zero-dimensional model can be expressed as:

$$Q_s = f(R_s) \tag{9}$$

2.3.3 Coronary Stenosis Model

The previously established coronary stenosis model was adopted to simulate the resistance generated by the stenotic coronary artery (**Fig. 4C-D**) [36]. In order to model a stenosis resistance similar to that of the three-dimensional CFD, we first computed the stenosis resistance of 3028 ideal stenosis models using the three-dimensional CFD approach, which was divided into training, validation and test sets with approximate ratios 8:1:1 [36]. Then, we adopted a back-propagation neural network (BPNN) architecture to describe complex nonlinear relationships between input and output variables. The input characteristic parameters of the model were six stenotic geometric parameters (including stenosis degree, stenosis entrance length, stenosis exit length, stenosis minimum length, stenosis entrance area and stenosis minimum area, **Fig. 4C**) and hyperemic coronary flow, and the output characteristic parameter was stenosis resistance (**Fig. 4D**). Six stenotic geometric parameters, hyperemic coronary flow and stenosis resistance calculated by three-dimensional CFD were used for training. Mean squared error was used as the loss function to evaluate the error between the predicted values from the network and the actual output data during the training process. Finally, the BPNN (i.e., coronary stenosis model, **Fig. 4D**) was established instead of three-dimensional CFD to predict stenosis resistance, and the accuracy of the BPNN had been verified by 30 personalized models [36]. The developed BPNN architecture consisted of one input layer, six hidden layers and one output layer, which was determined after hyperparameter adjustment [36]. For the personalized coronary stenosis model, the geometric parameters are constant, while stenosis resistance changes with the change of hyperemic coronary flow. Hence, the coronary stenosis model allowed to be expressed as:

$$R_s=f(Q_s) \tag{10}$$

2.3.4 Numerical Simulation

Coupling of coronary zero-dimensional model and coronary stenosis model enabled the determination of individualized stenosis resistance and hyperemic coronary flow. As mentioned above, the coronary zero-dimensional model was able to be expressed as $Q_s=f(R_s)$, while the coronary stenosis model was able to be represented as $R_s=f(Q_s)$. For the two models, the coronary zero-dimensional model provided hyperemic coronary flow for the coronary stenosis model, while the coronary stenosis model provided stenosis resistance for the coronary zero-dimensional model. Hence, the two models were iteratively calculated, and convergence was reached when $|Q_s'-Q_s| \leq 0.0001$ ml/s, where Q_s' is the new hyperemic coronary flow and Q_s is the previous hyperemic coronary flow. This allowed simultaneous determination of individualized stenosis resistance and hyperemic coronary flow to simulate patient-specific coronary pressure and flow.

Further, the distal coronary pressure (P_d) was computed according to hyperemic microcirculation resistance and hyperemic coronary flow.

$$P_d=Q_s \cdot R_{m\text{-}hyp} \tag{11}$$

Finally, cFFR was calculated by distal coronary pressure and aortic pressure:

$$\text{cFFR}=\frac{P_d}{P_a} \tag{12}$$

The cFFR calculated with $P_{a\text{-}res}$ and $P_{a\text{-}hyp}$ as inlet boundary conditions were denoted as cFFR_r and cFFR_h, respectively. The reconstruction and segmentation of coronary anatomical model (including the measurement of geometric parameters) was carried out using Mimics Research version 20.0 under the guidance of clinical cardiologists. The coronary stenosis model was implemented in Python 3.7, using Keras and Tensorflow libraries. Other modeling and simulation were performed using Matlab version R2018b.

2.4 Statistical Analysis

All statistical analyses were carried out using IBM SPSS Statistics version 25.0 and MedCalc version 19.4.0. Normal distribution was tested using the Shapiro-Wilk test. Categorical variables are represented as frequencies and percentages, with continuous variables as mean ± standard deviation (SD). Pearson correlation coefficient was used to analyze and evaluate the relationship between cFFR and iFFR. Bland-Altman analysis and 95% limits of agreement were adopted to assess the agreement of cFFR and iFFR. The receiver operating characteristic (ROC) curves were compared using iFFR < 0.80 as the reference standard. The area under the receiver operating characteristic curve (AUC) was computed using the DeLong method to evaluate the diagnostic performance of cFFR and CCTA. Diagnostic accuracy, sensitivity, specificity, positive predictive value (PPV), negative predictive value (NPV), positive likelihood ratio (LR+), and negative likelihood ratio (LR−) with 95% confidence interval (CI) were calculated for cFFR < 0.80 and CCTA stenosis degree $\geq 70\%$.

3. Results

3.1 Patient Characteristics

The study population consisted of 75 patients (75 vessels). Baseline characteristics of patients and lesions are summarized in **Table 1**. The average age of patients was 61.6 ± 10.1 years old, including 46 males and 29 females. Among the 75 vessels, 62 (82.7%) lesions were located in left anterior descending arteries, 3 (4.0%) were in left circumflex arteries, and 10

(13.3%) were in right coronary arteries. Among the 75 lesions, 16 (21.3%) coronary stenosis was caused by non-calcified plaques, 30 (40.0%) coronary stenosis was caused by calcified plaques, and the rest were caused by mixed plaques. CCTA stenosis degree ≥ 70% was mostly caused by non-calcified plaques and mixed plaques, which may be because stable plaques (calcified plaques) generally less susceptible to increasing stenosis, while unstable plaques (non-calcified plaques and mixed plaques) are more likely to lead to acute stenosis and even vessel occlusion. Excluding the time spent on reconstruction and segmentation of the coronary anatomical model (about half an hour), the average calculation time of cFFR was less than 2 seconds.

3.2 Correlation and Agreement of cFFR to iFFR

Four representative examples are displayed in **Fig. 5**, and details of the four cases are shown in **Table 2**. As shown in **Fig. 5**, Cases 1-3 demonstrate the success of prediction, where the clinical measurement results are consistent with the simulation results (both either show ischemia, or both show no ischemia). Case 4 shows the failure of prediction, where the clinical measurement results (iFFR > 0.8, no ischemia) are inconsistent with the simulation calculation results (cFFR < 0.8, ischemia).

The scatterplot reveals a good correlation between cFFR and iFFR (**Fig. 6**). Pearson correlation coefficients of $cFFR_r$ and $cFFR_h$ with iFFR were $r = 0.89$ ($p < 0.001$) and $r = 0.90$ ($p < 0.001$), respectively. The Bland-Altman analysis demonstrates a slight systematic difference between cFFR and iFFR (**Fig. 7**). The mean differences between $cFFR_r$ and $cFFR_h$ with iFFR were 0.003 (95% limits of agreement: -0.21 to 0.14) and -0.009 (95% limits of agreement: -0.25 to 0.17), respectively.

3.3 Diagnostic Performance of cFFR versus CCTA for Diagnosis of Ischemia-Producing Lesions

Fig. 8 illustrates the ROC curve of cFFR and CCTA in the diagnosis of ischemic coronary stenosis. The results demonstrated that the AUC of $cFFR_r$, $cFFR_h$ and CCTA were 0.960 (95% CI: 0.888 to 0.992, $P < 0.001$), 0.960 (95% CI: 0.888 to 0.992, $P < 0.001$) and 0.889 (95% CI: 0.795 to 0.950, $P < 0.001$), respectively. **Figs. 8B-D** show that in selected samples, the proposed simplified model exhibited better diagnostic performance for coronary stenosis caused by non-calcified plaques and mixed plaques. **Table 3** lists the diagnostic characteristics of $cFFR < 0.80$ and CCTA stenosis degree ≥ 70% for detecting significant stenosis. The diagnostic accuracy, sensitivity, specificity, PPV, NPV, LR (+), LR (−) of $cFFR_r$ and $cFFR_h$ were 90.7%, 95.0%, 89.1%, 76.0%, 98.0%, 8.7, 0.1 and 92.0%, 95.0%, 90.9%, 79.2%, 98.0%, 10.5, 0.1, respectively. The performances of $cFFR_r$ and $cFFR_h$ were superior to CCTA for diagnosing ischemic lesions, the latter of which demonstrated an accuracy, sensitivity, specificity, PPV, NPV, LR (+), LR (−) of 78.7%, 80.0%, 78.2%, 57.1%, 91.5%, 3.7, 0.3, respectively.

4. Discussion

We successfully developed a simplified model to rapidly predict FFR and verified the accuracy of the model. The novelty of the model mainly lies in taking the stenotic coronary artery as the region of interest, simplifying the process of model analysis, and reducing the computational cost by simplifying the three-dimensional model to a zero-dimensional model. In addition, considering that ML technology is capable of extracting rich information from data, we combine a zero-dimensional model with the stenosis model based on ML to ensure the accuracy of the model. The average computation time is less than 2 seconds, which is feasible in a clinical environment. It is suitable for individualized patients with a stenosis of 30%-90%. The proposed simplified model thus has potential in clinical application for the detection of ischemic stenosis.

4.1 Model Analysis

4.1.1 Boundary Conditions

In the current study, two inlet boundary conditions, $P_{a\text{-}res}$ and $P_{a\text{-}hyp}$, were considered, and the outlet boundary condition adopted $R_{m\text{-}hyp}$, which is commonly used in the literature [9,23]. To ensure the accuracy of the model, the actual measured pulsatile aortic pressure should be used as the inlet boundary condition. Previous studies have naturally produced pulsatile aortic pressure through the interaction between heart model and systemic circulation model [9,23,24]. However, the pulsatile aortic pressure cannot be obtained non-invasively. Therefore, this study only used the stable aortic pressure for simulation. It is feasible to use the aortic pressure estimated by MAP (i.e., $P_{a\text{-}res}$) as an inlet boundary condition, which has been verified by previous studies [9,35]. Yet, the measurement of clinical FFR is performed under hyperemic conditions [37]. To be physiologically realistic, the $P_{a\text{-}hyp}$ was also considered as the inlet boundary condition in this study.

In theory, there is a pressure drop in the coronary segment from the aorta to the inlet of the stenosis, meaning that the pressure at the inlet of the stenosis is actually lower than the aortic pressure. In this study, the aortic pressure was set as the inlet boundary condition, which may lead to a higher simulated distal pressure of the stenosis, resulting in a higher simulated FFR. Nevertheless, compared with the pressure drop caused by the stenosis, the pressure drop caused by the coronary artery from the aorta to the inlet of the stenosis can be considered negligible. Our results also showed that the effect of this part of the pressure drop is negligible.

We compared the diagnostic performance of two stable inlet boundary conditions, $P_{a\text{-}res}$ and $P_{a\text{-}hyp}$. Results manifested that the accuracy, specificity and PPV of $P_{a\text{-}hyp}$ were slightly higher than those of $P_{a\text{-}res}$ in the selected patient cohort (accuracy: 92.0% vs 90.7%; specificity: 90.9% vs 89.1%; PPV: 79.2% vs 76.0%). Although using a stable aortic pressure boundary condition may reduce the accuracy of the model compared to the actual pulsatile aortic pressure waveform, the stable blood flow model still guarantees the accuracy of the cFFR calculation as shown by our results.

4.1.2 Coronary Zero-Dimensional Model

The zero-dimensional model has been widely used in the modeling of cardiovascular mechanics, which allows simulation of coronary flow and pressure [23–28]. In the present study, we took the stenotic single-vessel coronary artery as the region of interest, assuming that the coronary artery was healthy and normal, and adopted a coronary zero-dimensional model to describe the healthy coronary artery. Flow resistance is simulated by resistance, flow rate is simulated by current and blood pressure is simulated by voltage. Furthermore, the coronary resistance computation and flow distribution adopted the methods proposed by Taylor et al. [9]. The coronary three-dimensional model was simplified to coronary zero-dimensional model, which avoided the solution of the three-dimensional flow field and greatly reduced the time required for analysis.

In a previous study, in order to simulate various parts of physiologically realistic circulatory system, a complete lumped parameter model of the coronary artery and cardiovascular system was established, which permitted simulating physiologically realistic pressure and flow of the coronary artery [24]. In this study, on the one hand, we considered that the topology of the coronary artery is parallel, which means that the parallel branches do not affect each other, and the downstream coronary arteries have almost no effect on the upstream coronary arteries. On the other hand, the blood vessel of interest is the stenotic coronary artery. Therefore, it is feasible to take the stenotic single-vessel coronary artery as the region of interest. Only the stenotic coronary artery is analyzed, avoiding calculation of the solution of other branches, thus greatly reducing the simulation time.

4.1.3 Coronary Stenosis Model

Since the zero-dimensional model cannot describe the geometric characteristics of the three-dimensional coronary artery, we additionally evaluated the stenosis resistance generated by the stenotic coronary artery to accurately simulate the coronary flow. In a previous study, we employed an experimentally validated analytical model related to stenotic geometric parameters and flow rate [38]. In this analytical model, the stenosis resistance was estimated by a theoretical formula. In it the geometric parameters of stenosis were obtained by manual measurement of the stenotic coronary artery from a three-dimensional reconstruction. To simulate the stenotic resistance consistent with the three-dimensional CFD to ensure the accuracy of the calculation model, this study adopted a BPNN (i.e., coronary stenosis model) to simulate the hemodynamics of stenotic coronary arteries [36]. This BPNN was trained on a large number of stenotic geometric parameters, hyperemic coronary flow and stenosis resistance predicted by the three-dimensional CFD, and allowed simulation of the stenosis resistance similar to the three-dimensional CFD, which had been verified by 30 personalized models [36]. Accordingly, the coronary stenosis model allows prediction of the stenosis resistance instead of the three-dimensional CFD, thereby ensuring a physiologically realistic simulation of the coronary flow.

4.2 Model Comparison

Previous studies of fast computed CT-FFR exhibited good diagnostic performance. Siemens Healthcare used a hybrid reduced-order CFD model to quickly calculate CT-FFR (cFFR, Siemens) from CCTA images [19]. The cFFR demonstrated a moderate correlation with iFFR, with the Pearson correlation coefficient ranging from 0.59 to 0.74, and the range of AUC for detected ischemia-causing stenosis was 0.83 to 0.91 [15,39–42]. The analysis time of cFFR varied from 30 to 120 min [15,39–42]. Subsequently, Toshiba Medical proposed a CT-FFR (CT-FFR, Toshiba) technology using a reduced-order model for structure and fluid analysis with a non-Newtonian fluid model [20,21]. The correlation between CT-FFR and iFFR was 0.57, the accuracy of CT-FFR was 83.9%, and AUC was 0.88 [17]. The mean analysis time was 27.07 ± 7.54 min [17]. In addition, Siemens Healthcare presented a new version of CT-FFR (cFFR, Siemens) based on ML [22]. These studies showed that the accuracy of ML-based cFFR ranged from 78% to 93%, and the correlation between ML-based cFFR and iFFR ranged from 0.62 to 0.85. The AUC of ML-based cFFR ranged from 0.84 to 0.94. The operating time of ML-based cFFR varied from 10 to 50 min [16,43,44]. Moreover, United-Imaging Healthcare developed a CT-FFR (uCT-FFR, United-Imaging) method using TAG to define the outlet boundary conditions [18]. The diagnostic accuracy, sensitivity, specificity, PPV and NPV of uCT-FFR were 91%, 89%, 91%, 86% and 94%, respectively. The mean operation time of uCT-FFR was 11.0 ± 2.8 min [18].

Similar to these previous methods, our approach provides a non-invasive evaluation of FFR based on conventional CCTA images. Excluding the time spent on the generation of coronary anatomical model in the preprocessing stage, the previous Heartflow CT-FFR required several hours of simulation on a supercomputer to obtain the FFR, with diagnostic accuracy between 73% and 87.4%, and AUC between 0.81 and 0.92 [12–14]. The previous fast algorithm used a standard desktop computer with a computing time of 5-15 min, AUC of 0.83 to 0.94, and diagnostic accuracy of 74.6% to 93% [15–18]. Our method only needed a simulation on an ordinary computer (Intel Core i7-7700 CPU at 3.6 GHz) and obtained the FFR in less than 2 seconds. This may be due to the reduction of the region of interest to include only the stenotic coronary artery and the simplification of the model to a zero-dimensional circuit structure for analysis, thus greatly reducing the computational cost. Compared with previous methods, our approach is computationally efficient in terms of execution speed and hardware requirements, which may be suitable for clinical timeliness requirements. In addition, the diagnostic accuracy of our algorithm (90.7% for $cFFR_r$ and 92.0% for $cFFR_h$) is in the same range as that of the previously published results. This may be because we used a coronary stenosis model based on ML to simulate the resistance generated by stenotic segments. The existing results prove that our method not only meets the clinical timeliness requirements (calculation speed), but also ensures the accuracy of FFR prediction (calculation accuracy), which means that this study has potential application value for clinical non-invasive diagnosis of ischemia-causing coronary stenosis.

4.3 Limitations and Perspectives

This study has several limitations. First, this study was a single-center retrospective study with a limited sample size for model validation. Moreover, since it has not been formally used in clinical practice, this study lacks follow-up data regarding the use of efficient CT-FFR to guide patient treatment. Multicenter prospective studies are needed to verify the feasibility of the model for application in large-scale experiments. In addition, the geometric features of the three-dimensional model were obtained by manual measurement, which may produce errors and lead to the reduction of the accuracy of the model. Furthermore, statistical assumptions were used in the determination of coronary model parameters, such as application of allometric scaling law (flow rate is proportional to the cubic of diameter) and quantification of $R_{m\text{-}hyp}$ (resistance is reduced to 0.24 times of $R_{m\text{-}res}$). These parameters vary across patients. Finally, the current method of segmentation is still time consuming, thus, it is necessary to develop an automatic model segmentation, avoid errors caused by manual intervention, and enable fast segmentation while ensuring model accuracy.

5. Conclusions

We have proposed a simplified model for the calculation of FFR, which improves the calculation speed by simplifying the coronary model and ensures the model accuracy by applying ML to predict stenosis resistance. The feasibility and accuracy of the simplified model were validated by comparison with invasive clinical measurements. The results demonstrate that the model not only guarantees the accuracy of FFR calculation, but also produces the fast prediction of FFR. This has potential application value in the diagnosis of clinical myocardial ischemia, and may be used to assist the detection of stenotic coronary artery with hemodynamic significance in the future.

Acknowledgements

The authors gratefully acknowledge Dr. Liu and his team (Department of Cardiology, Peking University People's Hospital, Beijing, China) for conducting the clinical experiment and providing the clinical data.

Funding

This study was supported by the National Natural Science Foundation of China (Grant No. 11832003, 12202022, 32271361, 12102014), the National Key Research and Development Program of China (Grant No. 2021YFA1000200, 2021YFC1000202, and 2020YFC2004400), China Postdoctoral Science Foundation (Grant No. 2022M710281), Beijing Postdoctoral Research Foundation (Grant No. 2022-ZZ-035).

Competing Interests

The authors have reported that they have no relationships relevant to the contents of this paper to disclose.

Data Availability

The data underlying this article will be shared on reasonable request to the corresponding author.

Author Contributions

All authors made a substantial contribution either to the conception or design of the study (YF, BL, LZ, YL), the acquisition of data (YF, YH, TW, HG, JM), the analysis and interpretation of data (YF, RF, QF), the drafting of the manuscript (YF), or critical revision of the manuscript for important intellectual content (BL, RF, LZ, HY, GB, YL). All authors approved the final version to be published and agreed to be accountable for all aspects of the work.

References

[1] J.K. Min, D.S. Berman, M.J. Budoff, F.A. Jaffer, J. Leipsic, M.B. Leon, G.B.J. Mancini, L. Mauri, R.S. Schwartz, L.J. Shaw, Rationale and design of the DeFACTO (Determination of Fractional Flow Reserve by Anatomic Computed Tomographic AngiOgraphy) study, J. Cardiovasc. Comput. Tomogr. 5 (2011) 301–309. https://doi.org/10.1016/j.jcct.2011.08.003.

[2] S. Seitun, A. Clemente, C.D. Lorenzi, S. Benenati, D. Chiappino, C. Mantini, A.I. Sakellarios, F. Cademartiri, G.P. Bezante, I. Porto, Cardiac CT perfusion and FFRCTA: pathophysiological features in ischemic heart disease, Cardiovascular Diagnosis and Therapy. 10 (2020) 1954–1978. https://doi.org/10.21037/cdt-20-414.

[3] F.E. Fossan, L.O. Müller, J. Sturdy, A.T. Bråten, A. Jørgensen, R. Wiseth, L.R. Hellevik, Machine learning augmented reduced-order models for FFR-prediction, Comput. Methods Appl. Mech. Eng. 384 (2021) 113892. https://doi.org/10.1016/j.cma.2021.113892.

[4] J.K. Min, C.A. Taylor, S. Achenbach, B.K. Koo, J. Leipsic, B.L. Nørgaard, N.J. Pijls, B. De Bruyne, Noninvasive Fractional Flow Reserve Derived From Coronary CT Angiography, JACC: Cardiovascular Imaging. 8 (2015) 1209–1222. https://doi.org/10.1016/j.jcmg.2015.08.006.

[5] B. De Bruyne, N.H.J. Pijls, B. Kalesan, E. Barbato, P.A.L. Tonino, Z. Piroth, N. Jagic, S. Möbius-Winkler, G. Rioufol, N. Witt, P. Kala, P. MacCarthy, T. Engström, K.G. Oldroyd, K. Mavromatis, G. Manoharan, P. Verlee, O. Frobert, N. Curzen, J.B. Johnson, P. Jüni,

W.F. Fearon, Fractional Flow Reserve–Guided PCI versus Medical Therapy in Stable Coronary Disease, N. Engl. J. Med. 367 (2012) 991–1001. https://doi.org/10.1056/NEJMoa1205361.

[6] L.X. Van Nunen, F.M. Zimmermann, P.A.L. Tonino, E. Barbato, A. Baumbach, T. Engstrøm, V. Klauss, P.A. MacCarthy, G. Manoharan, K.G. Oldroyd, P.N. Ver Lee, M. Van'T Veer, W.F. Fearon, B. De Bruyne, N.H.J. Pijls, Fractional flow reserve versus angiography for guidance of PCI in patients with multivessel coronary artery disease (FAME): 5-year follow-up of a randomised controlled trial, Lancet. 386 (2015) 1853–1860. https://doi.org/10.1016/S0140-6736(15)00057-4.

[7] W.F. Fearon, T. Nishi, B. De Bruyne, D.B. Boothroyd, E. Barbato, P. Tonino, P. Jüni, N.H.J. Pijls, M.A. Hlatky, Clinical Outcomes and Cost-Effectiveness of Fractional Flow Reserve–Guided Percutaneous Coronary Intervention in Patients With Stable Coronary Artery Disease: Three-Year Follow-Up of the FAME 2 Trial (Fractional Flow Reserve Versus Angiography for Multivessel Evaluation), Circulation. 137 (2018) 480–487. https://doi.org/10.1161/CIRCULATIONAHA.117.031907.

[8] P.D. Morris, F.N. Van De Vosse, P.V. Lawford, D.R. Hose, J.P. Gunn, "Virtual" (Computed) Fractional Flow Reserve, JACC: Cardiovascular Interventions. 8 (2015) 1009–1017. https://doi.org/10.1016/j.jcin.2015.04.006.

[9] C.A. Taylor, T.A. Fonte, J.K. Min, Computational Fluid Dynamics Applied to Cardiac Computed Tomography for Noninvasive Quantification of Fractional Flow Reserve, J. Am. Coll. Cardiol. 61 (2013) 2233–2241. https://doi.org/10.1016/j.jacc.2012.11.083.

[10] R. Pandey, M. Kumar, J. Majdoubi, M. Rahimi-Gorji, V.K. Srivastav, A review study on blood in human coronary artery: Numerical approach, Comput. Methods Programs Biomed. 187 (2020) 105243. https://doi.org/10.1016/j.cmpb.2019.105243.

[11] J. Chen, L.H. Wetzel, K.L. Pope, L.J. Meek, T. Rosamond, C.M. Walker, FFRCT: Current status, Am. J. Roentgenol. 216 (2021) 640–648. https://doi.org/10.2214/AJR.20.23332.

[12] B.-K. Koo, A. Erglis, J.-H. Doh, D.V. Daniels, S. Jegere, H.-S. Kim, A. Dunning, T. DeFrance, A. Lansky, J. Leipsic, J.K. Min, Diagnosis of Ischemia-Causing Coronary Stenoses by Noninvasive Fractional Flow Reserve Computed From Coronary Computed Tomographic Angiograms, J. Am. Coll. Cardiol. 58 (2011) 1989–1997. https://doi.org/10.1016/j.jacc.2011.06.066.

[13] J.K. Min, J. Leipsic, M.J. Pencina, D.S. Berman, B.-K. Koo, C. Van Mieghem, A. Erglis, F.Y. Lin, A.M. Dunning, P. Apruzzese, M.J. Budoff, J.H. Cole, F.A. Jaffer, M.B. Leon, J. Malpeso, G.B.J. Mancini, S.-J. Park, R.S. Schwartz, L.J. Shaw, L. Mauri, Diagnostic Accuracy of Fractional Flow Reserve From Anatomic CT Angiography, Jama. 308 (2012) 1237. https://doi.org/10.1001/2012.jama.11274.

[14] B.L. Nørgaard, J. Leipsic, S. Gaur, S. Seneviratne, B.S. Ko, H. Ito, J.M. Jensen, L. Mauri, B. De Bruyne, H. Bezerra, K. Osawa, M. Marwan, C. Naber, A. Erglis, S.-J. Park, E.H. Christiansen, A. Kaltoft, J.F. Lassen, H.E. Bøtker, S. Achenbach, Diagnostic Performance of Noninvasive Fractional Flow Reserve Derived From Coronary Computed Tomography Angiography in Suspected Coronary Artery Disease, J. Am. Coll. Cardiol. 63 (2014) 1145–1155. https://doi.org/10.1016/j.jacc.2013.11.043.

[15] A. Coenen, M.M. Lubbers, A. Kurata, A. Kono, A. Dedic, R.G. Chelu, M.L. Dijkshoorn, F.J. Gijsen, M. Ouhlous, R.-J.M. Van Geuns, K. Nieman, Fractional Flow Reserve Computed from Noninvasive CT Angiography Data: Diagnostic Performance of an On-Site Clinician-operated Computational Fluid Dynamics Algorithm, Radiology. 274 (2015) 674–683. https://doi.org/10.1148/radiol.14140992.

[16] J. Röther, M. Moshage, D. Dey, C. Schwemmer, M. Tröbs, F. Blachutzik, S. Achenbach, C. Schlundt, M. Marwan, Comparison of invasively measured FFR with FFR derived from coronary CT angiography for detection of lesion-specific ischemia: Results from a PC-based prototype algorithm, J. Cardiovasc. Comput. Tomogr. 12 (2018) 101–107. https://doi.org/10.1016/j.jcct.2018.01.012.

[17] B.S. Ko, J.D. Cameron, R.K. Munnur, D.T.L. Wong, Y. Fujisawa, T. Sakaguchi, K. Hirohata, J. Hislop-Jambrich, S. Fujimoto, K. Takamura, M. Crossett, M. Leung, A. Kuganesan, Y. Malaiapan, A. Nasis, J. Troupis, I.T. Meredith, S.K. Seneviratne, Noninvasive CT-Derived FFR Based on Structural and Fluid Analysis, JACC: Cardiovascular Imaging. 10 (2017) 663–673. https://doi.org/10.1016/j.jcmg.2016.07.005.

[18] C.X. Tang, C.Y. Liu, M.J. Lu, U.J. Schoepf, C. Tesche, R.R. Bayer, H.T. Hudson, X.L. Zhang, J.H. Li, Y.N. Wang, C.S. Zhou, J.Y. Zhang, M.M. Yu, Y. Hou, M.W. Zheng, B. Zhang, D.M. Zhang, Y. Yi, Y. Ren, C.W. Li, X. Zhao, G.M. Lu, X.H. Hu, L. Xu, L.J. Zhang, CT FFR for Ischemia-Specific CAD With a New Computational Fluid Dynamics Algorithm, JACC: Cardiovascular Imaging. 13 (2020) 980–990. https://doi.org/10.1016/j.jcmg.2019.06.018.

[19] L. Itu, Puneet. Sharma, V. Mihalef, A. Kamen, C. Suciu, D. Lomaniciu, A patient-specific reduced-order model for coronary circulation, in: 2012 9th IEEE International Symposium on Biomedical Imaging (ISBI), IEEE, Barcelona, Spain, 2012: pp. 832–835. https://doi.org/10.1109/ISBI.2012.6235677.

[20] K. Hirohata, A. Kano, A. Goryu, J. Ooga, T. Hongo, S. Higashi, Y. Fujisawa, S. Wakai, K. Arakita, Y. Ikeda, S. Kaminaga, B.S. Ko, S.K. Seneviratne, A novel CT-FFR method for the coronary artery based on 4D-CT image analysis and structural and fluid analysis, in: C. Hoeschen, D. Kontos, T.G. Flohr (Eds.), Medical Imaging 2015: Physics of Medical Imaging, SPIE, Orlando, Florida, United States, 2015: p. 94122O. https://doi.org/10.1117/12.2081674.

[21] M. Kato, K. Hirohata, A. Kano, S. Higashi, A. Goryu, T. Hongo, S. Kaminaga, Y. Fujisawa, Fast CT-FFR Analysis Method for the Coronary Artery Based on 4D-CT Image Analysis and Structural and Fluid Analysis, in: ASME 2015 International Mechanical Engineering Congress and Exposition, ASME, Houston, Texas, USA, 2015: p. V003T03A023. https://doi.org/10.1115/IMECE2015-51124.

[22] L. Itu, S. Rapaka, T. Passerini, B. Georgescu, C. Schwemmer, M. Schoebinger, T. Flohr, P. Sharma, D. Comaniciu, A machine-learning approach for computation of fractional flow reserve from coronary computed tomography, J. Appl. Physiol. 121 (2016) 42–52. https://doi.org/10.1152/japplphysiol.00752.2015.

[23] H.J. Kim, I.E. Vignon-Clementel, J.S. Coogan, C.A. Figueroa, K.E. Jansen, C.A. Taylor, Patient-Specific Modeling of Blood Flow and Pressure in Human Coronary Arteries, Ann.

Biomed. Eng. 38 (2010) 3195–3209. https://doi.org/10.1007/s10439-010-0083-6.

[24] Y. Feng, R. Fu, B. Li, N. Li, H. Yang, J. Liu, Y. Liu, Prediction of fractional flow reserve based on reduced-order cardiovascular model, Comput. Methods Appl. Mech. Eng. 400 (2022) 115473. https://doi.org/10.1016/j.cma.2022.115473.

[25] P.D. Morris, A. Narracott, H. von Tengg-Kobligk, D.A.S. Soto, S. Hsiao, A. Lungu, P. Evans, N.W. Bressloff, P.V. Lawford, D.R. Hose, J.P. Gunn, Computational fluid dynamics modelling in cardiovascular medicine, Heart. 102 (2016) 18–28. https://doi.org/10.1136/heartjnl-2015-308044.

[26] H.J. Kim, I.E. Vignon-Clementel, C.A. Figueroa, J.F. LaDisa, K.E. Jansen, J.A. Feinstein, C.A. Taylor, On Coupling a Lumped Parameter Heart Model and a Three-Dimensional Finite Element Aorta Model, Ann. Biomed. Eng. 37 (2009) 2153–2169. https://doi.org/10.1007/s10439-009-9760-8.

[27] M.E. Moghadam, I.E. Vignon-Clementel, R. Figliola, A.L. Marsden, A modular numerical method for implicit 0D/3D coupling in cardiovascular finite element simulations, J. Comput. Phys. 244 (2013) 63–79. https://doi.org/10.1016/j.jcp.2012.07.035.

[28] B. Li, H. Wang, G. Li, J. Liu, Z. Zhang, K. Gu, H. Yang, A. Qiao, J. Du, Y. Liu, A patient-specific modelling method of blood circulatory system for the numerical simulation of enhanced external counterpulsation, J. Biomech. 111 (2020) 110002. https://doi.org/10.1016/j.jbiomech.2020.110002.

[29] S.L. Brunton, B.R. Noack, P. Koumoutsakos, Machine Learning for Fluid Mechanics, Annu. Rev. Fluid Mech. 52 (2020) 477–508. https://doi.org/10.1146/annurev-fluid-

010719-060214.

[30] H. Moradi, A. Al-Hourani, G. Concilia, F. Khoshmanesh, F.R. Nezami, S. Needham, S. Baratchi, K. Khoshmanesh, Recent developments in modeling, imaging, and monitoring of cardiovascular diseases using machine learning, Biophys. Rev. 15 (2023) 19–33. https://doi.org/10.1007/s12551-022-01040-7.

[31] G.L.D. Maria, H.M. Garcia-Garcia, R. Scarsini, A. Hideo-Kajita, N.G. López, A.M. Leone, G. Sarno, J. Daemen, E. Shlofmitz, A. Jeremias, M. Tebaldi, H.G. Bezerra, S. Tu, P.A. Lemos, Y. Ozaki, K. Dan, C. Collet, A.P. Banning, E. Barbato, N.P. Johnson, R. Waksman, Novel Indices of Coronary Physiology: Do We Need Alternatives to Fractional Flow Reserve?, Circulation: Cardiovascular Interventions. 13 (2020) e008487. https://doi.org/10.1161/CIRCINTERVENTIONS.119.008487.

[32] J. Jiang, C. Li, Y. Hu, C. Li, J. He, X. Leng, J. Xiang, J. Ge, J. Wang, A novel CFD-based computed index of microcirculatory resistance (IMR) derived from coronary angiography to assess coronary microcirculation, Comput. Methods Programs Biomed. 221 (2022) 106897. https://doi.org/10.1016/j.cmpb.2022.106897.

[33] J.M. Zhang, G. Chandola, R.-S. Tan, P. Chai, L.L.S. Teo, R. Low, J.C. Allen, W. Huang, J.M. Fam, C.Y. Chin, A.S.L. Wong, A.F. Low, G.S. Kassab, T. Chua, S.Y. Tan, S.T. Lim, L. Zhong, Quantification of effects of mean blood pressure and left ventricular mass on noninvasive fast fractional flow reserve, American Journal of Physiology - Heart and Circulatory Physiology. 319 (2020) H360–H369. https://doi.org/10.1152/ajpheart.00135.2020.

[34] N. Li, B. Li, J. Liu, Y. Feng, L. Zhang, J. Liu, Y. Liu, The quantitative relationship between coronary microcirculatory resistance and myocardial ischemia in patients with coronary artery disease, J. Biomech. 140 (2022) 111166. https://doi.org/10.1016/j.jbiomech.2022.111166.

[35] W. He, L. Yu, W. Qin, Y. Wang, K. Wang, W. Guo, S. Wang, A modified method of noninvasive computed tomography derived fractional flow reserve based on the microvascular growth space, Computer Methods and Programs in Biomedicine. 221 (2022) 106926. https://doi.org/10.1016/j.cmpb.2022.106926.

[36] H. Sun, J. Liu, Y. Feng, X. Xi, K. Xu, L. Zhang, J. Liu, B. Li, Y. Liu, Deep learning-based prediction of coronary artery stenosis resistance, American Journal of Physiology-Heart and Circulatory Physiology. 323 (2022) H1194–H1205. https://doi.org/10.1152/ajpheart.00269.2022.

[37] L. Yu, W. Guo, W. He, W. Qin, M. Zeng, S. Wang, A novel method for calculating CTFFR based on the flow ratio between stenotic coronary and healthy coronary, Comput. Methods Programs Biomed. 233 (2023) 107469. https://doi.org/10.1016/j.cmpb.2023.107469.

[38] Y. Huo, M. Svendsen, J.S. Choy, Z.-D. Zhang, G.S. Kassab, A validated predictive model of coronary fractional flow reserve, Journal of The Royal Society Interface. 9 (2012) 1325–1338. https://doi.org/10.1098/rsif.2011.0605.

[39] D.H. Yang, Y.-H. Kim, J.H. Roh, J.-W. Kang, J.-M. Ahn, J. Kweon, J.B. Lee, S.H. Choi, E.-S. Shin, D.-W. Park, S.-J. Kang, S.-W. Lee, C.W. Lee, S.-W. Park, S.-J. Park, T.-H. Lim, Diagnostic performance of on-site CT-derived fractional flow reserve versus CT perfusion,

European Heart Journal - Cardiovascular Imaging. 18 (2017) 432–440. https://doi.org/10.1093/ehjci/jew094.

[40] S. Baumann, R. Wang, U.J. Schoepf, D.H. Steinberg, J.V. Spearman, R.R. Bayer, C.W. Hamm, M. Renker, Coronary CT angiography-derived fractional flow reserve correlated with invasive fractional flow reserve measurements – initial experience with a novel physician-driven algorithm, Eur. Radiol. 25 (2015) 1201–1207. https://doi.org/10.1007/s00330-014-3482-5.

[41] A. Coenen, M.M. Lubbers, A. Kurata, A. Kono, A. Dedic, R.G. Chelu, M.L. Dijkshoorn, R.-J.M. Van Geuns, M. Schoebinger, L. Itu, P. Sharma, K. Nieman, Coronary CT angiography derived fractional flow reserve: Methodology and evaluation of a point of care algorithm, J. Cardiovasc. Comput. Tomogr. 10 (2016) 105–113. https://doi.org/10.1016/j.jcct.2015.12.006.

[42] M. Kruk, Ł. Wardziak, M. Demkow, W. Pleban, J. Pręgowski, Z. Dzielińska, M. Witulski, A. Witkowski, W. Rużyłło, C. Kępka, Workstation-Based Calculation of CTA-Based FFR for Intermediate Stenosis, JACC: Cardiovascular Imaging. 9 (2016) 690–699. https://doi.org/10.1016/j.jcmg.2015.09.019.

[43] A. Coenen, Y.-H. Kim, M. Kruk, C. Tesche, J. De Geer, A. Kurata, M.L. Lubbers, J. Daemen, L. Itu, S. Rapaka, P. Sharma, C. Schwemmer, A. Persson, U.J. Schoepf, C. Kepka, D. Hyun Yang, K. Nieman, Diagnostic Accuracy of a Machine-Learning Approach to Coronary Computed Tomographic Angiography–Based Fractional Flow Reserve: Result From the MACHINE Consortium, Circulation: Cardiovascular Imaging. 11 (2018)

e007217. https://doi.org/10.1161/CIRCIMAGING.117.007217.

[44] C. Tesche, C.N. De Cecco, S. Baumann, M. Renker, T.W. McLaurin, T.M. Duguay, R.R. Bayer, D.H. Steinberg, K.L. Grant, C. Canstein, C. Schwemmer, M. Schoebinger, L.M. Itu, S. Rapaka, P. Sharma, U.J. Schoepf, Coronary CT Angiography–derived Fractional Flow Reserve: Machine Learning Algorithm versus Computational Fluid Dynamics Modeling, Radiology. 288 (2018) 64–72. https://doi.org/10.1148/radiol.2018171291.

Figure Legends

Fig. 1 Coronary anatomical model

A Coronary artery tree; **B** Geometric model describing the anatomical features of stenosis

Fig. 2 Coronary physiological model

Q_{cor} indicates total coronary flow; CO, cardiac output; R_m, coronary microvascular resistance; and d, coronary vessel diameter

Fig. 3 Schematic diagram of coronary artery structure

A represents the inlet of coronary branch, 1 and 2 represent the nodes of coronary branches, and 1a, 2a, 2b represent the outlets of coronary branches

Fig. 4 Computational model of cFFR

A Schematic diagram of three-dimensional stenotic coronary artery; **B** Coronary zero-dimensional model (electrical analog model); **C** Geometric model describing the anatomical features of stenosis; **D** Coronary stenosis model (BPNN). The input features of the BPNN are: stenosis degree, stenosis entrance length, stenosis exit length, stenosis minimum length, stenosis entrance area and stenosis minimum area and hyperemic coronary flow, and the output feature is stenosis resistance.

P_a indicates aortic pressure; P_d, distal coronary pressure; P_v, venous pressure; Q_s, hyperemic coronary flow; R_s, stenosis resistance; R_m, coronary microvascular resistance; $P_{a\text{-}res}$, resting aortic pressure; $P_{a\text{-}hyp}$, hyperemic aortic pressure; $R_{m\text{-}hyp}$, hyperemic coronary microvascular resistance; and BPNN, back-propagation neural network model

Fig. 5 Representative cases of cFFR simulation

cFFR indicates computational fractional flow reserve; iFFR, invasive fractional flow reserve; $cFFR_r$, cFFR with resting aortic pressure as inlet boundary conditions; and $cFFR_h$, cFFR with hyperemic aortic pressure as inlet boundary conditions

Fig. 6 Scatter plots show correlation between cFFR and iFFR

Pearson correlation coefficient of cFFR and iFFR with **A** resting aortic pressure and **B** hyperemic aortic pressure as inlet boundary conditions. Abbreviations as in **Fig. 5**

Fig. 7 Bland-Altman plots of cFFR and iFFR

Agreement between cFFR and iFFR with **A** resting aortic pressure and **B** hyperemic aortic pressure as inlet boundary conditions. Abbreviations as in **Fig. 5**

Fig. 8 ROC curves of cFFR and CCTA

The AUC of $cFFR_r$, $cFFR_h$, and CCTA for discrimination of ischemic coronary stenosis (iFFR < 0.80). **A** All lesions; **B** Non-calcified plaque; **C** Calcified plaque; **D** Mixed plaque.

ROC indicates receiver operating characteristic; CCTA, coronary computed tomography angiography; AUC, area under the receiver-operating characteristic curve; other abbreviations as in **Fig. 5**

Fig. 1

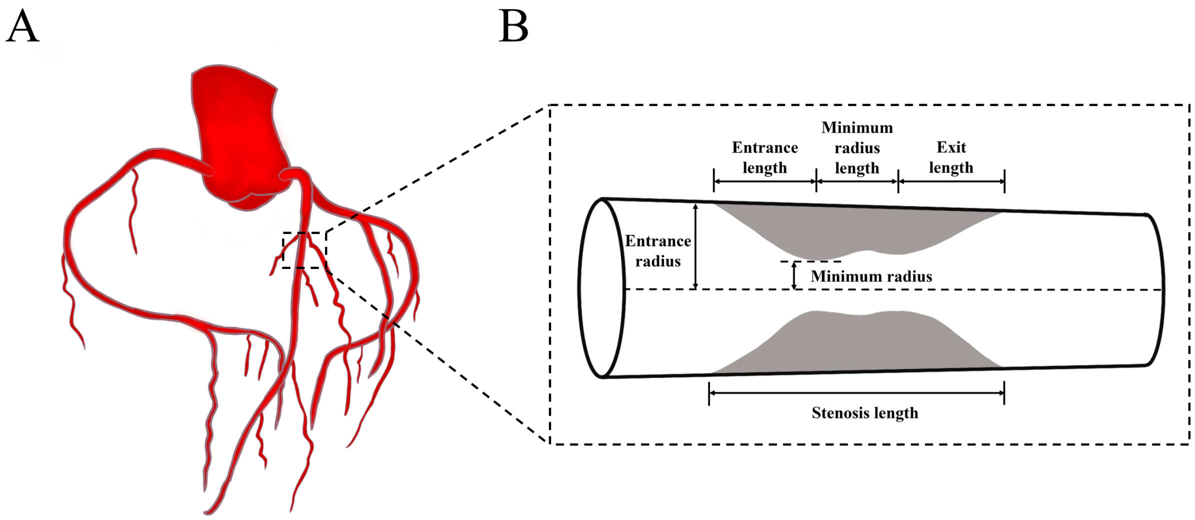
A
B
Entrance length
Minimum radius length
Exit length
Entrance radius
Minimum radius
Stenosis length

Fig. 2

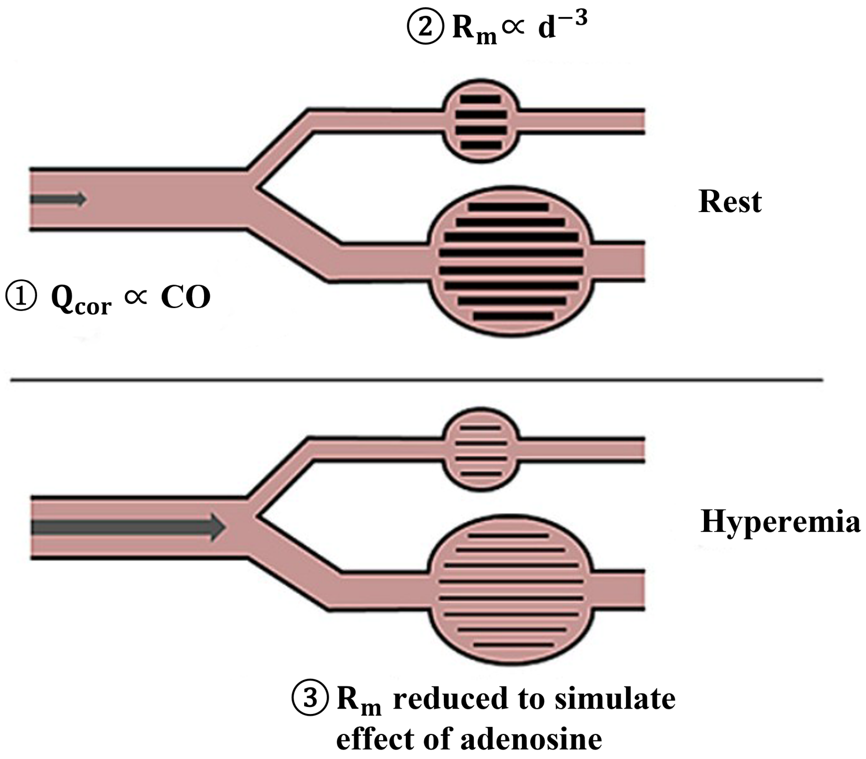
② $R_m \propto d^{-3}$
Rest
① $Q_{cor} \propto CO$
Hyperemia
③ R_m reduced to simulate effect of adenosine

Fig. 3

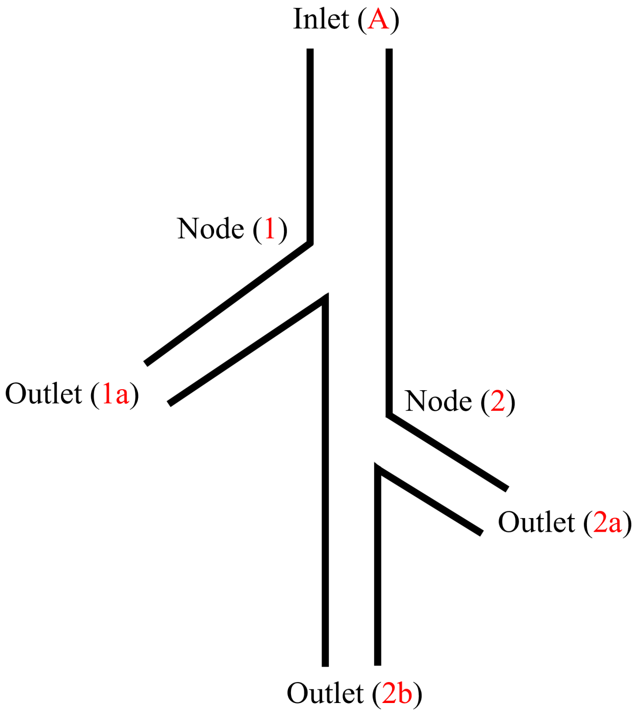

Fig. 4

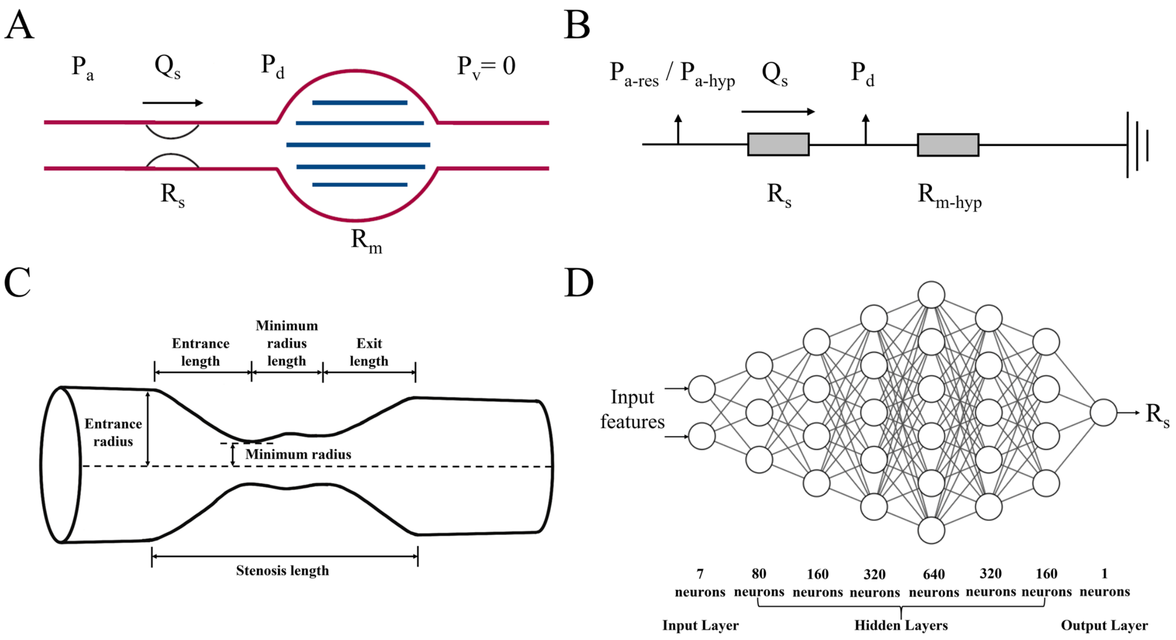
A
P_a
Q_s
P_d
$P_v = 0$
R_s
R_m
B
$P_{a\text{-res}}$ / $P_{a\text{-hyp}}$
Q_s
P_d
R_s
$R_{m\text{-hyp}}$
C
Entrance length
Minimum radius length
Exit length
Entrance radius
Minimum radius
Stenosis length
D
Input features
R_s
7 neurons
80 neurons
160 neurons
320 neurons
640 neurons
320 neurons
160 neurons
1 neurons
Input Layer
Hidden Layers
Output Layer

Fig. 5

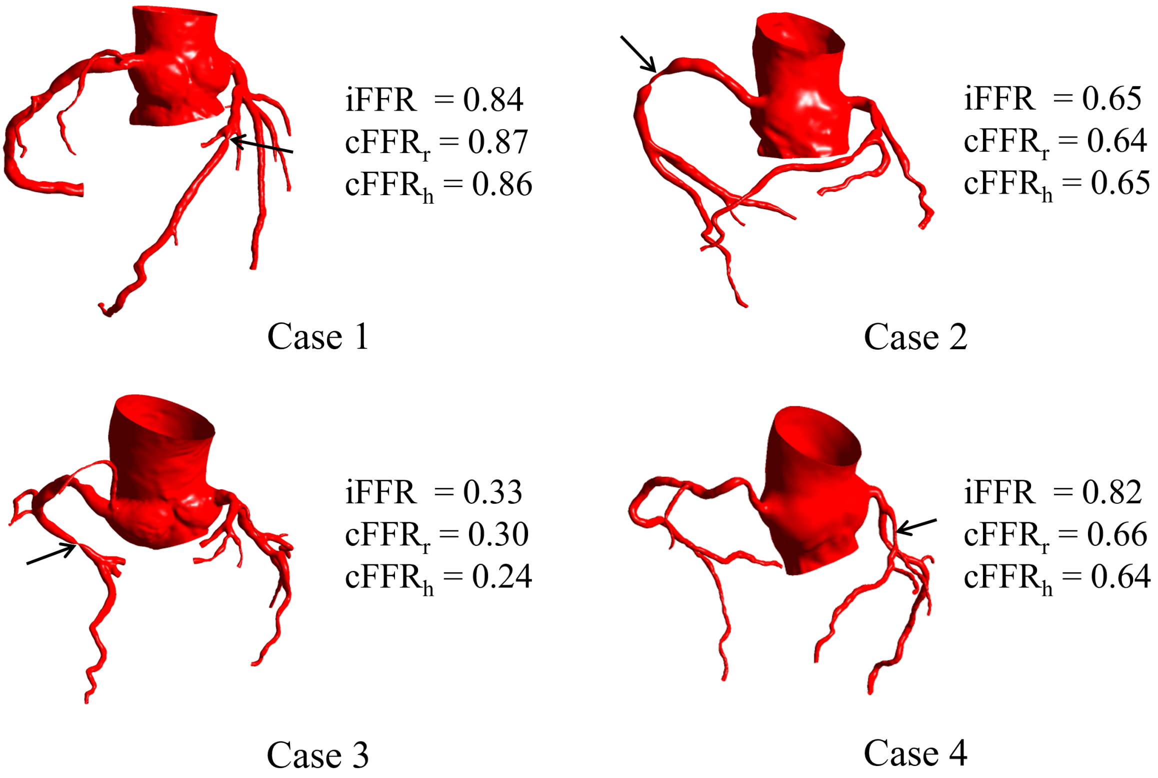
iFFR = 0.84
$\text{cFFR}_r = 0.87$
$\text{cFFR}_h = 0.86$
Case 1
iFFR = 0.65
$\text{cFFR}_r = 0.64$
$\text{cFFR}_h = 0.65$
Case 2
iFFR = 0.33
$\text{cFFR}_r = 0.30$
$\text{cFFR}_h = 0.24$
Case 3
iFFR = 0.82
$\text{cFFR}_r = 0.66$
$\text{cFFR}_h = 0.64$
Case 4

Fig. 6

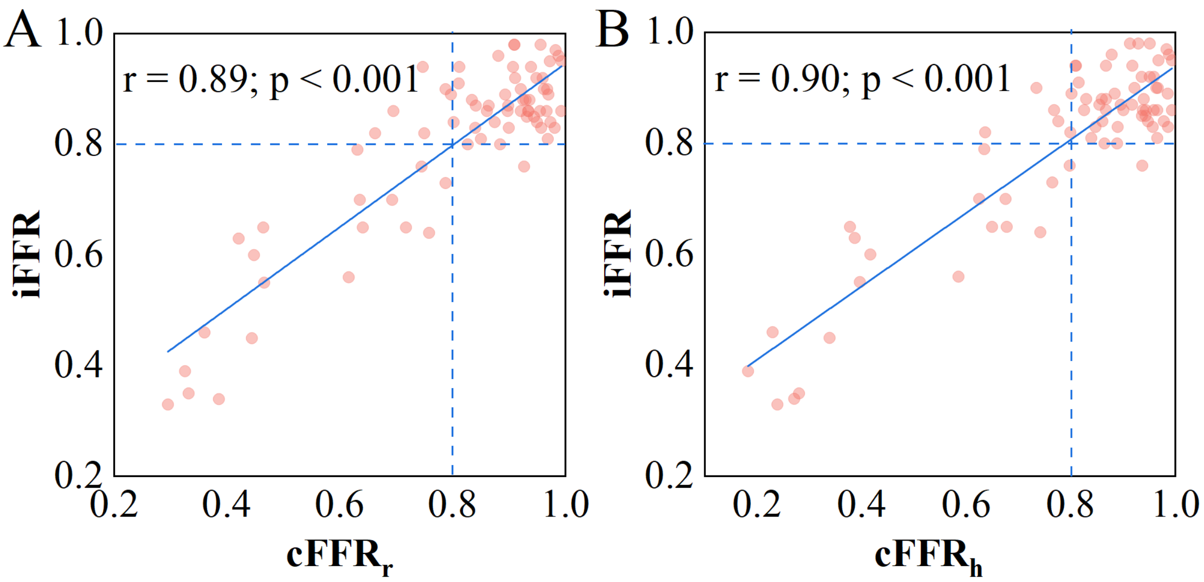
A
r = 0.89; p < 0.001
iFFR
1.0
0.8
0.6
0.4
0.2
0.2
0.4
0.6
0.8
1.0
cFFR_r
B
r = 0.90; p < 0.001
iFFR
1.0
0.8
0.6
0.4
0.2
0.2
0.4
0.6
0.8
1.0
cFFR_h

Fig. 7

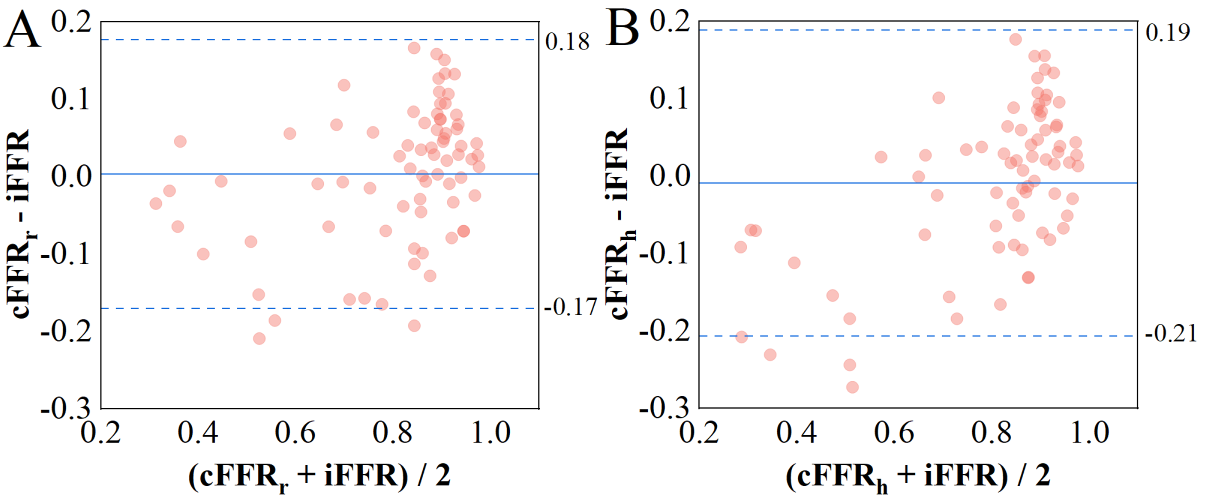
A
B
cFFR$_r$ - iFFR
(cFFR$_r$ + iFFR) / 2
cFFR$_h$ - iFFR
(cFFR$_h$ + iFFR) / 2
0.2
0.1
0.0
-0.1
-0.2
-0.3
0.2
0.4
0.6
0.8
1.0
0.18
-0.17
0.19
-0.21

Fig. 8

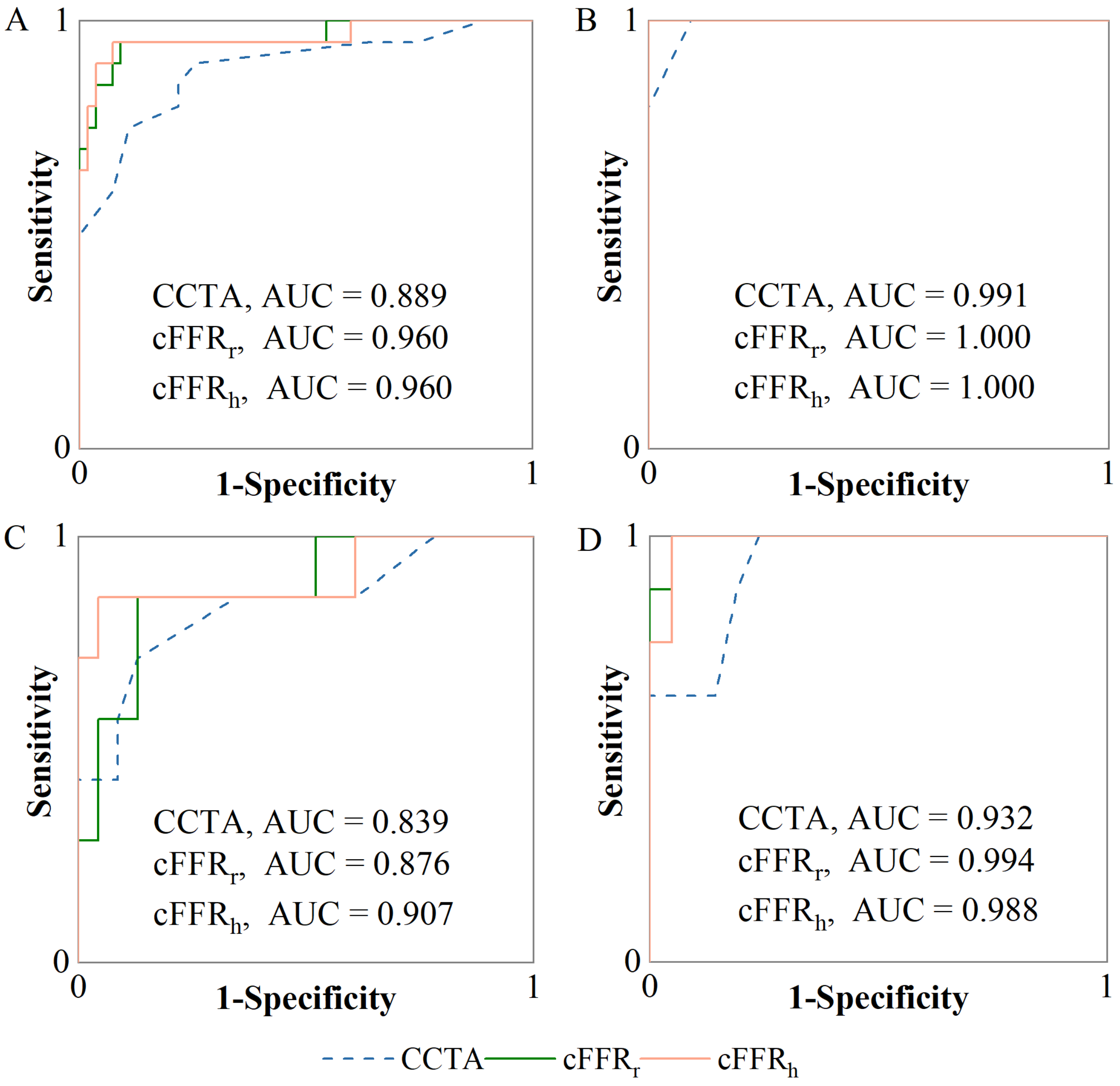
A
B
C
D
1
0
Sensitivity
1-Specificity
CCTA, AUC = 0.889
cFFR$_r$, AUC = 0.960
cFFR$_h$, AUC = 0.960
CCTA, AUC = 0.991
cFFR$_r$, AUC = 1.000
cFFR$_h$, AUC = 1.000
CCTA, AUC = 0.839
cFFR$_r$, AUC = 0.876
cFFR$_h$, AUC = 0.907
CCTA, AUC = 0.932
cFFR$_r$, AUC = 0.994
cFFR$_h$, AUC = 0.988
CCTA
cFFR$_r$
cFFR$_h$

Tables

Table 1 Baseline characteristics

Parameter	All patients/lesions (N = 75)	Non-calcified plaque (N = 16)	Calcified plaque (N = 30)	Mixed plaque (N = 29)
Age (years)	61.6 ± 10.1	56.1 ± 13.0	62.5 ± 8.2	63.8 ± 9.3
Female	29 (38.7)	6 (37.5)	14 (46.7)	9 (31.0)
SBP (mmHg)	132.4 ± 15.5	130.4 ± 15.5	132.2 ± 15.5	133.7 ± 15.9
DBP (mmHg)	78.4 ± 11.6	77.4 ± 6.9	81.0 ± 12.8	76.2 ± 12.1
HR (beats/min）	72.2 ± 12.8	77.1 ± 13.3	69.6 ± 12.0	72.3 ± 13.0
CO (L/min)	4.6 ± 1.1	4.6 ± 1.2	4.7 ± 1.1	4.4 ± 1.1
Lesion location				
LAD	62 (82.7)	13 (81.3)	26 (86.7)	23 (79.3)
LCX	3 (4.0)	1 (6.3)	1 (3.3)	1 (3.4)
RCA	10 (13.3)	2 (12.5)	3 (10.0)	5 (17.2)
CCTA stenosis degree ≥ 70%	28 (37.3)	10 (62.5)	5 (16.7)	13 (44.8)
iFFR < 0.80	20 (26.7)	5 (31.3)	7 (23.3)	8 (27.6)

Values are mean ± SD or n (%).

SBP indicates systolic blood pressure; DBP, diastolic blood pressure; HR, heart rate; CO, cardiac output; LAD, left anterior descending artery; LCX, left circumflex artery; RCA, right coronary artery; CCTA, coronary computed tomography angiography; and iFFR, invasive fractional flow reserve

Table 2 Physiological parameters and simulation results of representative examples

Patient	Gender	Age (years)	HR (beats/min)	SBP (mmHg)	DBP (mmHg)	CO (L/min)	Lesion location	CCTA stenosis degree	iFFR	cFFR$_r$	cFFR$_h$
Case 1	Male	64	66	106	66	3.43	LAD	0.6	0.84	0.87	0.86
Case 2	Female	64	88	137	77	3.90	RCA	0.9	0.65	0.64	0.65
Case 3	Male	75	70	115	71	4.21	RCA	0.9	0.33	0.30	0.24
Case 4	Male	61	68	123	77	3.81	LAD	0.75	0.82	0.66	0.64

cFFR indicates computational fractional flow reserve; cFFR$_r$, cFFR with resting aortic pressure as inlet boundary conditions; cFFR$_h$, cFFR with hyperemic aortic pressure as inlet boundary conditions; other abbreviations as in **Table 1**

Table 3 Diagnostic characteristics of cFFR and CCTA compared with iFFR

	cFFR$_r$ < 0.80	cFFR$_h$ < 0.80	CCTA Stenosis Degree≥ 70%
TP	19	19	16
FP	6	5	12
TN	49	50	43
FN	1	1	4
Accuracy (%)	90.7 (81.7-96.2)	92.0 (83.4-97.0)	78.7 (67.7-87.3)
Sensitivity (%)	95.0 (75.1-99.9)	95.0 (75.1-99.9)	80.0 (56.3-94.3)
Specificity (%)	89.1 (77.8-95.9)	90.9 (80.0-97.0)	78.2 (65.0-88.2)
PPV (%)	76.0 (59.6-87.2)	79.2 (62.1-89.8)	57.1 (43.6-69.7)
NPV (%)	98.0 (87.9-99.7)	98.0 (88.1-99.7)	91.5 (81.6-96.3)
LR (+)	8.7 (4.1-18.7)	10.5 (4.5-24.2)	3.7 (2.1-6.3)
LR (−)	0.1 (0.0-0.4)	0.1 (0.0-0.4)	0.3 (0.1-0.6)

Values in parentheses are 95% confidence interval.

TP indicates true positive; FP, false positive; TN, true negative; FN, false negative; PPV, positive predictive value; NPV, negative predictive value; LR (+), positive likelihood ratio; and LR (–), negative likelihood ratio; other abbreviations as in **Tables 1** and **2**